Role of a Polycyclic Aromatic Hydrocarbon Bay Region Ring in Modulating DNA Adduct Structure: The Non-Bay Region (8*S*,9*R*,10*S*,11*R*)-N^6-[11-(8,9,10,11-Tetrahydro-8,9,10-trihydroxybenz[*a*]anthracenyl)]-2′-deoxyadenosyl Adduct in Codon 61 of the Human *N-ras* Protooncogene†

Zhijun Li, Hye-Young Kim, Pamela J. Tamura, Constance M. Harris, Thomas M. Harris, and Michael P. Stone*

Department of Chemistry and Center in Molecular Toxicology, Vanderbilt University, Nashville, Tennessee 37235

Received July 13, 1999; Revised Manuscript Received August 27, 1999

ABSTRACT: The structure of the non-bay region (8*S*,9*R*,10*S*,11*R*)-N^6-[11-(8,9,10,11-tetrahydro-8,9,10-trihydroxybenz[*a*]anthracenyl)]-2′-deoxyadenosyl adduct at X^6 of 5′-d(CGGAC<u>XA</u>AGAAG)-3′•5′-d(CTTCTTGTCCG)-3′, incorporating codons 60, 61 (underlined), and 62 of the human *N-ras* protooncogene, was determined. Molecular dynamics simulations were restrained by 475 NOEs from ^{1}H NMR. The benz[*a*]anthracene moiety intercalated above the 5′-face of the modified base pair and from the major groove. The duplex suffered distortion at and immediately adjacent to the adduct site. This was evidenced by the disruption of the Watson−Crick base pairing for X^6•T^{17} and A^7•T^{16} and the increased rise of 7.7 Å between base pairs C^5•G^{18} and X^6•T^{17}. Increased disorder was observed as excess line width of proton resonances near the lesion site. Comparison with the bay region benzo[*a*]pyrene [Zegar, I. S., Kim, S. J., Johansen, T. N., Horton, P. J., Harris, C. M., Harris, T. M., and Stone, M. P. (1996) *Biochemistry 35*, 6212−6224] and bay region benz[*a*]anthracene [Li, Z., Mao, H., Kim, H.-Y., Tamura, P. J., Harris, C. M., Harris, T. M., and Stone, M. P. (1999) *Biochemistry 38*, 2969−2981] adducts with the corresponding stereochemistry and at the same site shows that this non-bay region benz[*a*]anthracene lesion assumes different base pair geometry, in addition to exhibiting greater disorder. These differences are attributed to the loss of the bay region ring. The results suggest the bay region ring contributes to base stacking interactions at the lesion site. These structural differences between the non-bay and bay region lesions are correlated with site-specific mutagenesis data. The bay region benzo[*a*]pyrene and bay region benz[*a*]anthracene adducts were poorly replicated in vivo, and induced A → G mutations. In contrast, the non-bay region benz[*a*]anthracene adduct was easily bypassed in vivo and was nonmutagenic.

Benz[*a*]anthracene (BA)[1] is a significant component of coal tar, atmospheric pollution (*1*, *2*), automobile exhaust, and cigarette smoke (*3*). It is a member of the polycyclic aromatic hydrocarbon (PAH) class of mutagens. The toxic effects of these chemicals have been recognized since Percival Pott's linkage between the incidence of scrotal cancer in chimney sweeps and occupational exposure to soot in the 18th century (*4*). Their genotoxicity is generally recognized to result from their stepwise oxidation by cytochromes P_{450} (*5*, *6*), generally to stereoisomeric "bay region" electrophilic diol epoxides. The epoxides adduct nucleophilic sites on the bases of DNA, especially guanine N^2 (*7*−*9*), but also other sites, including adenine N^6 (*10*, *11*). In most instances, including BA, PAH adducts at adenine N^6 are less abundant, compared to the corresponding guanine N^2 adducts. These adducts are nevertheless of interest as the minor adenine lesions may have disproportionate biological significance (*12*−*14*).

Benz[*a*]anthracene is somewhat less carcinogenic than benzo[*a*]pyrene (BP) or dibenz[*a*,*h*]anthracene (*15*, *16*). Of the stereoisomeric bay region BA diol epoxides, (1*R*,2*S*,3*S*,4*R*)-3,4-dihydroxy-1,2-epoxy-1,2,3,4-tetrahydrobenz[*a*]anthracene (DE2) has significant tumor-initiating activity in mouse skin and newborn mice (*17*). This diol epoxide has the same absolute configuration as the highly tumorigenic isomers of the BP and chrysene bay region diol epoxides. The bay region diol epoxides of BA are also mutagenic in bacterial strains and in V79-6 Chinese hamster lung cells (*18*−*20*).

† This work was supported by NIH Grant ES-05355. Funding for the NMR spectrometer was supplied by NIH Grant RR-05805 and the Vanderbilt Center in Molecular Toxicology, ES-00267. The National Magnetic Resonance Facility at Madison was funded by the University of Wisconsin, NSF Grants DMB-8415048 and BIR-9214394, NIH Grants RR-02301, RR-02781, and RR08438, and the U.S. Department of Agriculture.

* To whom correspondence should be addressed. Phone: (615) 322-2589. Fax: (615) 343-1234. E-mail: stone@toxicology.mc.vanderbilt.edu.

[1] Abbreviations: BA, benz[*a*]anthracene; BP, benzo[*a*]pyrene; BADE, BA diol epoxide; BPDE, BP diol epoxide; EDTA, ethylenediaminetetraacetic acid; HPLC, high-pressure liquid chromatography; NOE, nuclear Overhauser enhancement; NOESY, two-dimensional NOE spectroscopy; PAH, polycyclic aromatic hydrocarbon; TPPI, time-proportional phase increment; 1D, one-dimensional; 2D, two-dimensional. A right superscript refers to the numerical position in the sequence starting from the 5′-terminus of chain A and proceeding to the 3′-terminus of chain A and then from the 5′-terminus of chain B to the 3′-terminus of chain B. C2, C5, C6, C8, C1′, C2′, C2″, etc. represent specific carbon nuclei. H2, H5, H6, H8, H1′, H2′, H2″, etc. represent protons attached to these carbons.

10.1021/bi991607z CCC: $18.00
Published on Web 10/23/1999

Chart 1: *ras61* Oligodeoxynucleotide, Where X Is the (8*S*,9*R*,10*S*,11*R*)-N^6-[11-(8,9,10,11-Tetrahydro-8,9,10-trihydroxybenz[*a*]anthracenyl)]-2′-deoxyadenosyl Adduct[a]

ras codons

	60	61	62	
5′-	C^1 | G^2 G^3 A^4	| C^5 X^6 A^7	| G^8 A^9 A^{10}	| G^{11} -3′
3′-	G^{22} | $C^{21}C^{20}T^{19}$	| $G^{18}T^{17}T^{16}$	| $C^{15}T^{14}T^{13}$	| C^{12} -5′

[a] This adduct is located at the second position of codon 61, the (61,2) position.

The lower carcinogenicity of BA, as compared to that of the other PAH, may be due in part to a lower level of metabolism to the bay region diol epoxide (*21*−*23*).

It is generally recognized that bay region diol epoxides formed from oxidative metabolism of PAH compounds are more mutagenic than the corresponding non-bay region diol epoxides. However, the molecular basis for this observation has remained obscure. It was suggested that bay region diol epoxides exhibit enhanced reactivity with DNA (*24*). Alternatively, the structures of the resulting adducts might be more disruptive to DNA replication and repair, leading to greater numbers of mutations (*25*). We have used the *ras61* oligodeoxynucleotide 5′-d(CGGACAAGAAG)-3′·5′-d(CTTCTTGTCCG)-3′ (*26*) (Chart 1) to examine the solution conformation and mutagenic response of a series of bay region adenyl N^6 BP (*27*, *28*) and bay region BA (*29*) adducts which have been site-specifically located within the codon 61 sequence of the human *N-ras* protooncogene. Mutations within codon 61 cause oncogene activation (*30*). Others have examined the structures of a number of adenyl N^6 PAH adducts, both in the context of correct base pairing (*31*−*33*) and in the context of mispairing (*34*−*36*).

Because BA is activated to both bay and non-bay region diol epoxides (*5*), it provides a useful model for understanding PAH structure−activity relationships. Using a repair-deficient prokaryotic in vivo replication system, the bay region BA adducts were shown to be mutagenic (*37*). Site-specific mutagenesis demonstrated that the adenyl N^6 bay region BA RSRS(61,2) lesion induced A → G transitions, similar to the adenyl N^6 BP SRSR(61,2) adduct with corresponding stereochemistry (*38*). The mutagenic frequency was dependent on the stereochemistry about the adduct-forming bond, as well as the strain of *Escherichia coli* in which they were replicated. In contrast, the corresponding non-bay region adducts of BA were easily bypassed by *E. coli* replication complexes and were not mutagenic (*37*).

A nonbiomimetic approach to large-scale synthesis of PAH adducts at adenine N^6 (*39*) was extended to production of the (8*S*,9*R*,10*S*,11*R*)-N^6-[11-(8,9,10,11-tetrahydro-8,9,10-trihydroxybenz[*a*]anthracenyl)]-2′-deoxyadenosyl adduct (*40*−*42*) in the *ras61* oligodeoxynucleotide. This non-bay region BA adduct was site-specifically located in the oligodeoxynucleotide 5′-d(CGGACXAGAAG)-3′·5′-d(CTTCTTGTCCG)-3′, where X is the adducted adenine. This was named the non-bay region BA SRSR(61,2) adduct **1**. The relationship between this adduct and the bay region BP SRSR(61,2) **2** (*27*) and bay region BA RSRS(61,2) **3** (*29*) adducts is shown in Chart 2. Adduct **1** corresponds to the bay region BP adduct **2**, but without the bay region pyrenyl ring. Therefore, the non-bay region BA adduct provides a method for evaluating the structural role of the bay region pyrenyl ring of the corresponding bay region BP adduct.

In the work presented here, the solution structure of the non-bay region BA adduct **1** has been determined, and compared to the corresponding bay region BP (*27*) and BA (*29*) adducts **2** and **3**. Molecular dynamics calculations restrained by interproton distances obtained from ^{1}H nuclear Overhauser effects (*43*) demonstrate that the anthracenyl moiety intercalates above the 5′-face of the modified adenine from the major groove. This is similar to the bay region BA (*29*) and BP (*27*) adducts **2** and **3** with corresponding stereochemistry. However, adduct **1** exhibits poorer stacking with the neighboring base pairs X^6·T^{17} and C^5·G^{18}. Consequently, a geometry common to both adducts **2** and **3** in which the modified adenine shifts toward the minor groove reminiscent of a wobble A·C pair[2] is not observed for adduct **1**. Increased disorder is evident at and adjacent to adduct **1**, evidenced by ^{1}H spectral line width. These differences are attributed to the loss of the bay region ring as compared to adducts **2** (*29*) and **3** (*27*, *28*) with corresponding stereochemistry.

MATERIALS AND METHODS

Materials. The oligodeoxynucleotide 5′-d(CTTCTTGTCCG)-3′ was purchased from Midland Certified Reagent Co. (Midland, TX). The modified oligodeoxynucleotide 5′-d(CGGACXAGAAG)-3′ (Chart 1) was synthesized through a procedure in which (±)-amino triol derived from (±)-8β,9α-dihydroxy-10α,11α-epoxy-8,9,10,11-tetrahydrobenz[*a*]anthracene (DE2) was reacted with an oligodeoxynucleotide containing 6-fluoroadenosine at position X^6 (*40*, *41*, *44*). The modified oligodeoxynucleotide was purified from the reaction mixture by HPLC using a reverse-phase semi-preparative column (PRP-1; Hamilton Co., Reno, NV) equilibrated with 10 mM ethylenediamineacetate (pH 7.0). The oligodeoxynucleotide was eluted using a gradient consisting of 0 to 20% acetonitrile over the course of 20 min. Its identity was confirmed by circular dichroism spectroscopy, enzymatic digestion, and mass spectroscopy. The DNA was lyophilized and desalted on Sephadex G-25 (Amersham-Pharmacia, Piscataway, NJ).

NMR Samples. The oligodeoxynucleotide concentrations were determined from extinction coefficients of 1.09×10^5 M^{-1} cm^{-1} for modified and 9.24×10^4 M^{-1} cm^{-1} for the complementary strand, at 260 nm (*45*). The complementary oligodeoxynucleotides were mixed at a 1:1 molar ratio in 0.1 M NaCl, 10 mM NaH_2PO_4, and 50 μM Na_2EDTA at pH 7. The mixture was heated to 90 °C for 5 min, and was cooled to room temperature. DNA grade Bio-Gel hydroxylapatite (Bio-Rad Laboratories, Hercules, CA) (15 cm × 3.0 cm), eluted with a gradient from 10 to 200 mM NaH_2PO_4 (pH 7.0), was used for the separation of double- and single-stranded oligodeoxynucleotides. The duplex was lyophilized and dissolved in 0.5 mL of H_2O, and desalted on Sephadex

[2] I. S. Zegar, Z. Li, P. Chary, R. J. Jabil, A. G. McNees, M. O'Donnell, C. M. Harris, T. M. Harris, R. S. Lloyd, and M. P. Stone, manuscript in preparation.

Chart 2: (A) Non-Bay Region BA (8*S*,9*R*,10*S*,11*R*)-N^6-[11-(8,9,10,11-Tetrahydro-8,9,10-trihydroxybenz[*a*]anthracenyl)]-2′-deoxyadenosyl Adduct **1**, (B) Bay Region (−)-(7*S*,8*R*,9*S*,10*R*)-N^6-[10-(7,8,9,10-Tetrahydro-7,8,9-trihydroxybenzo[*a*]pyrenyl)]-2′-deoxyadenosyl Adduct **2**, and (C) Bay Region BA (1*R*,2*S*,3*R*,4*S*)-N^6-[1-(1,2,3,4-Tetrahydro-2,3,4-trihydroxybenz[*a*]anthracenyl)]-2′-deoxyadenosyl Adduct **3**

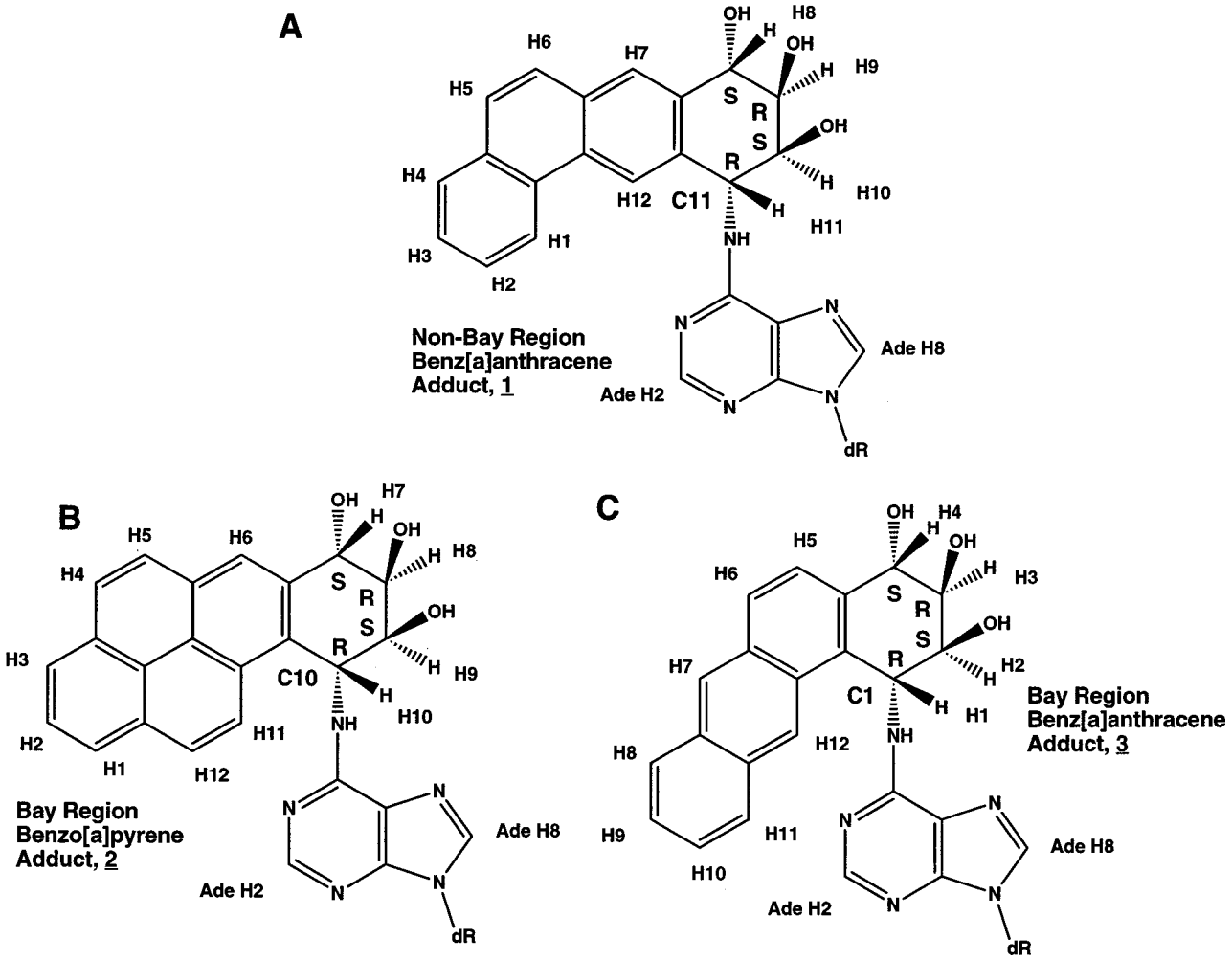

G-25 (70 cm × 1.5 cm). The sample was lyophilized and redissolved in 0.5 mL of NMR buffer containing 0.1 M NaCl, 10 mM NaH_2PO_4, and 50 μM Na_2EDTA at pH 7.0. The solution was lyophilized and exchanged three times with 99.96% D_2O. The strand concentration of the samples was ∼1.8 mM. The samples used for examining nonexchangeable protons were dissolved in 99.996% D_2O buffer. The samples used for the examination of the exchangeable protons were in buffer solution containing 9/1 H_2O/D_2O.

UV Melting. The experiments were carried out on a Varian Cary 4E spectrophotometer. The buffer was 10 mM sodium phosphate, 0.05 mM Na_2EDTA, and 1 M NaCl at pH 7.0. The buffer solution was degassed prior to the experiment. The concentrations were adjusted to 4.8×10^{-6} M in a 1 cm cuvette. The temperature was increased at a rate of 0.5 °C/min from 2 to 90 °C. The absorbance was measured at 260 nm. The melting temperatures of the native and modified oligodeoxynucleotides were calculated by determining the midpoints of the melting curves from the first-order derivatives.

NMR. Experiments were performed at ^{1}H frequencies of 750.13 and 500.13 MHz. For examining exchangeable protons, phase-sensitive NOESY experiments were carried out in 9/1 H_2O/D_2O buffer at a ^{1}H frequency of 500.13 MHz. The Watergate pulse sequence suppressed the water signal (*46*). The spectra were recorded at 5 °C with a mixing time of 250 ms. Phase-sensitive NOESY spectra used in the nonexchangeable proton resonance assignments were recorded at 20 °C using TPPI quadrature detection with a mixing time of 250 ms. To derive the distance restraints from NOESY experiments, three NOESY spectra were recorded consecutively at mixing times of 100, 150, and 250 ms. In these experiments, the data were recorded with 512 real data points in the t_1 dimension and 2048 real data points in the t_2 dimension. The relaxation delay was 2 s. The data were processed using FELIX (version 97.0, Molecular Simulations, Inc., San Diego, CA) on Silicon Graphics (Mountain View, CA) Octane workstations. The data in the t_1 dimension were zero-filled to give a matrix of 2K × 2K real points. A skewed sine-bell-square apodization function with a 90° phase shift was used in both dimensions.

NMR Distance Restraints. Footprints were drawn around the NOE cross-peaks for the NOESY spectrum measured at a mixing time of 250 ms to define the size and shape of the individual cross-peak using FELIX. The same set of footprints was applied to spectra measured at other mixing times. Cross-peak intensities were determined by volume integration of the areas under the footprints. The intensities were

combined as necessary with intensities generated from complete relaxation matrix analysis of a starting DNA structure to generate a hybrid intensity matrix (*47*). MARDIGRAS (version 3.0) (*48*, *49*) was used to refine the hybrid matrix by iteration, to optimize the agreement with experimental NOE intensities. We assumed the molecular motion was isotropic. Calculations generally requiring two to five cycles were performed using DNA starting models generated by INSIGHTII (version 97.0), and the three mixing time NOE experiments, with six τ_c values (2, 3, 4, 5, 6, and 7 ns). The resulting sets of distances were averaged to give the experimental NOE restraints used in subsequent molecular dynamics calculations (*43*). For partially overlapped cross-peaks, lower or upper error bounds on the resulting distances were increased.

Restrained Molecular Dynamics. Calculations were performed using X-PLOR (version 3.851) (*50*). The force field was derived from CHARMM (*51*) and adapted for restrained MD calculations of nucleic acids. The empirical energy function (*52*) was developed for nucleic acids and treated hydrogens explicitly. It consisted of energy terms for bonds, bond angles, torsion angles, tetrahedral and planar geometry, hydrogen bonding, and nonbonded interactions, including van der Waals and electrostatic forces. The van der Waals energy term was approximated using the Lennard-Jones potential energy function. The electrostatic term used the Coulomb function, based on a full set of partial charges (−1 per residue) and a distance-dependent dielectric constant of 4. The nonbonded pair list was updated if any atom moved more than 0.5 Å, and the cutoff radius for nonbonded interactions was 11 Å. All bond lengths involving hydrogens were kept fixed with the SHAKE algorithm (*53*). All calculations were performed in vacuo without explicit counterions. The integration time step was 1 fs.

The effective energy function included terms describing distance and dihedral restraints, which were in the form of square-well potentials (*54*). The distance restraints were divided into five classes based on the confidence factor obtained from MARDIGRAS. Additional empirical restraints were included for base pairs distal to the adduct site (i.e., other than the modified base pair and its nearest neighbors). The inclusion of these empirical restraints was based upon inspection of the NMR data. This showed the distal base pairs were essentially unchanged from the B-like geometry of the unmodified *ras61* duplex (*26*); i.e., the structural perturbations introduced by the BA were localized. The deoxyribose data for most distal base pairs were clearly consistent with the C2′-endo sugar ring conformation (*55*). Therefore, their deoxyribose rings were restrained to the C2′-endo conformation. Additionally, with the exception of the adduct site, the backbone torsion angles ϵ and ζ were restrained to 165 ± 35° and 245 ± 35°, respectively, consistent with B-like geometry. Likewise, with the exception of the adduct site and its 3′-adjacent base pairs, empirical Watson−Crick hydrogen bonding restraints between base pairs were used.

Sets of rMD calculations were performed using two starting structures, BA-Bi and BA-Ai, which were based on B-form and A-form DNA, respectively. Random velocities fitting a Maxwell−Boltzmann distribution were assigned. Calculations starting from BA-Bi were coupled to a heating bath with a target temperature of 1200 K. The force constants were 50 kcal mol^{-1} Å^{-2} for empirical hydrogen bonding, 10 kcal mol^{-1} Å^{-2} for sugar pucker, base pair planarity, and backbone torsion angle restraints, and 50, 45, 40, 35, and 30 kcal mol^{-1} Å^{-2} for the five classes of NOE restraints, respectively. The target temperature was reached in 5 ps and was maintained for 15 ps. The molecules were cooled to 300 K over the course of 5 ps and maintained at that temperature for 15 ps of equilibrium dynamics. The force constants for the five classes of NOE restraints were scaled up for 3−5 ps during the heating period to 200, 180, 160, 140, and 120 kcal mol^{-1} Å^{-2} in the order of confidence factor. These weights were maintained during the remainder of the heating period and for the first 2 ps of the equilibrium dynamics period. They were then scaled down to 100, 90, 80, 70, and 50 kcal mol^{-1} Å^{-2} in the order of confidence factor. The dihedral angle and base pair distance force constants were scaled up to 180 and 200 kcal mol^{-1} Å^{-2} at the same time as for the NOE restraints. They were scaled back to 70 and 50 kcal mol^{-1} Å^{-2}, also at the same time as the NOE restraints. Coordinate sets were archived every 0.1 ps, and 39 structures from the last 5 ps were averaged. These average rMD structures were subjected to 700 iterations of conjugate gradient minimization to obtain the final structures. During the final energy minimization, all the restraints were used. When BA-Ai was used as the starting stucture, a couple of changes about the simulated annealing protocol were made: the target temperature was 1100 K and was maintained for 6 ps, and the molecules were cooled to 300 K over the course of 2 ps. The rest parameters were kept the same. Back-calculation of theoretical NMR intensities from the emergent structures was performed using CORMA (version 4.0) (*47*). The structures were analyzed using DIALS AND WINDOWS 1.0 (*56*).

RESULTS

Thermal Stability. The thermal stability of the non-bay region BA adduct **1** was examined by UV melting studies that compared it with the unadducted *ras61* sequence. The measured T_m was 38 °C. This adduct destabilized the duplex, as indicated by a 16 °C reduction in T_m compared to that of the unmodified duplex. In comparison, the measured T_m for the bay region BP adduct **2** was 41 °C, a 13 °C destabilization. This compared to the T_m of the corresponding bay region BA adduct **3**, obtained under identical conditions, of 44 °C, a 10 °C reduction in T_m compared to that of the unmodified duplex. Thus, as compared to either the BP or the BA bay region adducts, the non-bay region BA adduct caused slightly greater destabilization of the DNA duplex. A series of ^{1}H spectra obtained from 10 to 35 °C indicated that 20 °C was the optimal temperature at which the duplex remained intact and the ^{1}H resonances were the sharpest and best resolved.

^{1}H Resonance Assignments. *(a) Nonexchangeable Protons*. Except at and adjacent to the lesion site, the spectrum was similar to that of the unmodified *ras61* oligomer (*26*). At the lesion site, the spectrum was similar to those of previously examined bay region adducts **2** (*27*) and **3** (*29*). For the modified strand, weaker NOE connectivities than anticipated for a B-DNA base step were observed between A^4 H1′ and C^5 H6 (Figure 1). No NOE connectivity was observed between C^5 H1′ and X^6 H8. This contrasted with the bay region BA adduct **3**, which exhibited a very weak

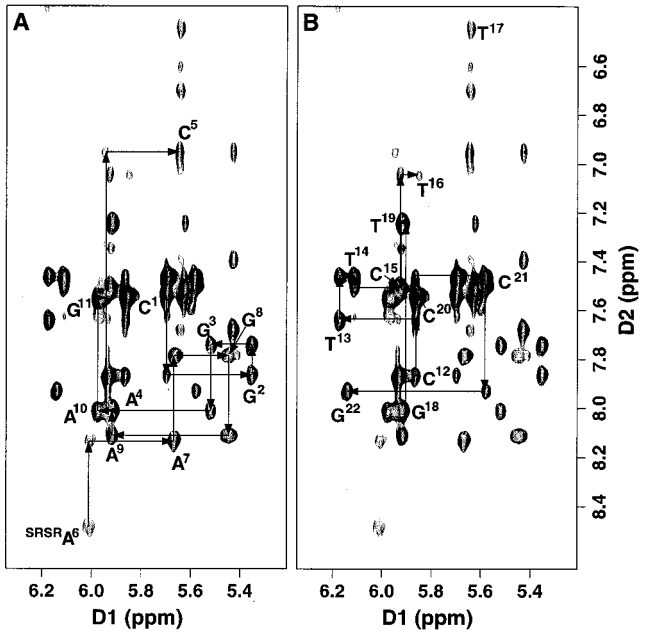

FIGURE 1: Expanded plots for the aromatic−anomeric region of the 750.13 MHz NOESY spectrum with a 250 ms mixing time. (A) Sequential NOE connectivities for the modified strand. (B) Sequential NOE connectivities for the complementary strand. The NOESY experiment was carried out at 20 °C.

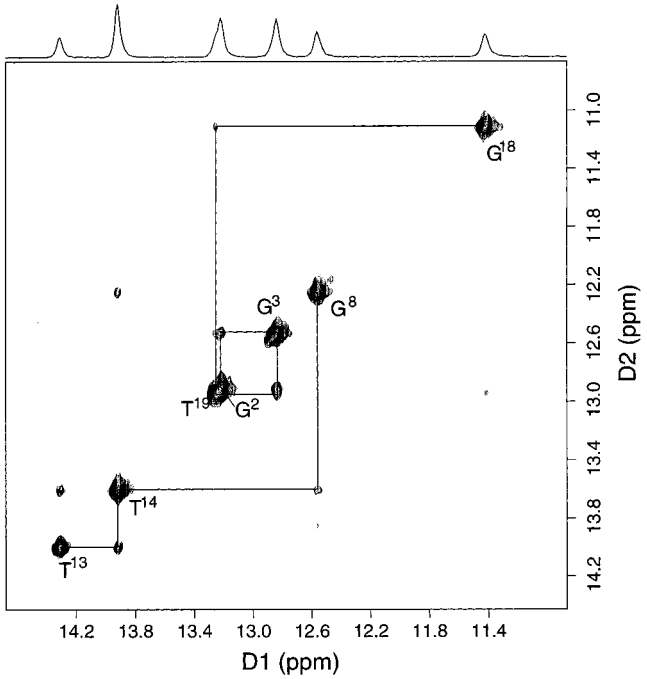

FIGURE 2: Expanded plot of a NOESY spectrum with a 250 ms mixing time showing the sequential NOE connectivities for the imino protons of base pairs G^2•C^{21} to A^{10}•T^{13}. The labels represent the imino proton of the designated base. Also shown is a 1D projection of the imino proton resonances. Both 1D and 2D experiments were carried out at 5 °C.

NOE between these protons (*29*). Likewise, the BP adduct **2** had also exhibited a weak NOE between these protons (*27*). Another difference between the previously examined bay region adducts of BA and BP and the non-bay region BA adduct was the intranucleotide NOE between X^6 H1′ and X^6 H8, which was weaker and broader than anticipated for B-DNA. In the complementary strand, the connectivity between T^{16} H1′ and T^{16} H6 was weaker than the corresponding NOEs observed for nucleotides far from the site of the lesion. This also contrasted with the BA (*29*) and BP (*27*) bay region adducts, for which this NOE was observed at normal intensity. No connectivities were observed between T^{16} H1′ and T^{17} H6 and between T^{17} H1′ and G^{18} H8. This was consistent with the previously examined bay region adducts. Five of the six cytosines exhibited cross-peaks in the expected region. The sixth, assigned to C^5, revealed a 0.5 ppm upfield shift of H5 relative to that normally observed for cytosine H5 protons. C^5 H6 also shifted upfield 0.2 ppm. Another large upfield shift was observed for T^{17} H6, which was at 6.5 ppm as compared to the usual 7−7.2 ppm range. These findings paralleled the earlier work with the bay region adducts. The assignments of the remainder of the sugar protons were determined from a DQF-COSY spectrum. No sequential NOEs were observed between C^5 H2″ and X^6 H8 and between T^{17} H2″ and G^{18} H8. The largest upfield shift of 1.4 ppm was observed for T^{17} CH_3. The chemical shifts of the nonexchangeable protons are listed in Table S1 of the Supporting Information.

(b) Exchangeable Protons. Assignments of the imino protons were made from NOE connectivities between adjacent base pairs and connectivities to the base-paired amino protons (*57*). An expanded region showing cross-peaks between the imino protons is given in Figure 2. Sequential assignments of the imino protons from base pairs G^2•C^{21} to C^5•G^{18} and G^8•C^{15} to A^{10}•T^{13} were obtained unequivocally. The spectrum was quite similar to those for the bay region adducts **2** (*27*) and **3** (*29*). The significant difference between the bay and non-bay region adducts was noted for the imino protons of T^{16} and T^{17}. For the non-bay region BA adduct, no NOE connectivities were observed between T^{16} N3H and T^{17} N3H or between T^{17} N3H and G^{18} N1H. In fact, both of these imino protons were exchange broadened to the point that they could no longer be observed in the ^{1}H spectrum. This implied substantial disruption of Watson−Crick hydrogen bonding at X^6•T^{17} and A^7•T^{16}. In contrast, for the bay region adducts (*27*, *29*), the NOE between T^{16} N3H and G^8 N1H had normal intensity. The NOE between T^{17} N3H and T^{16} N3H was weak (bay region BA) or missing (bay region BP) from the spectrum, due to exchange broadening of T^{17} N3H. With the exception of the 5′-terminal nucleotides C^1 and C^{12}, distinctive amino protons were observed for each cytosine, including C^5, the 5′-neighbor of the site of adduction. A downfield shift of 1.0 ppm for the hydrogen-bonded NH_{2a} and an upfield shift of 0.5 ppm for the non-hydrogen-bonded NH_{2b} were observed for C^5 relative to the chemical shifts observed for these resonances in the unmodified *ras61* duplex. Unusual shifts were not observed for the amino protons of other cytosines. The chemical shifts of the exchangeable protons are listed in Table S2 of the Supporting Information.

(c) Benz[a]anthracene Protons. An expanded region of the NOESY spectrum used for the assignment of BA protons is shown in Figure 3. The numbering scheme for the BA protons is shown in Chart 2. These resonances were dispersed over a 1 ppm chemical shift range, from 6.6 to 7.6 ppm. The H4, H5, H6, and H7 protons of the non-bay region BA adduct correspond to protons H3, H4, H5, and H6 of the bay region BP adduct (Chart 2). A similar pattern of chemical shifts for these protons was observed for the non-bay region BA adduct, compared with that of the corresponding bay

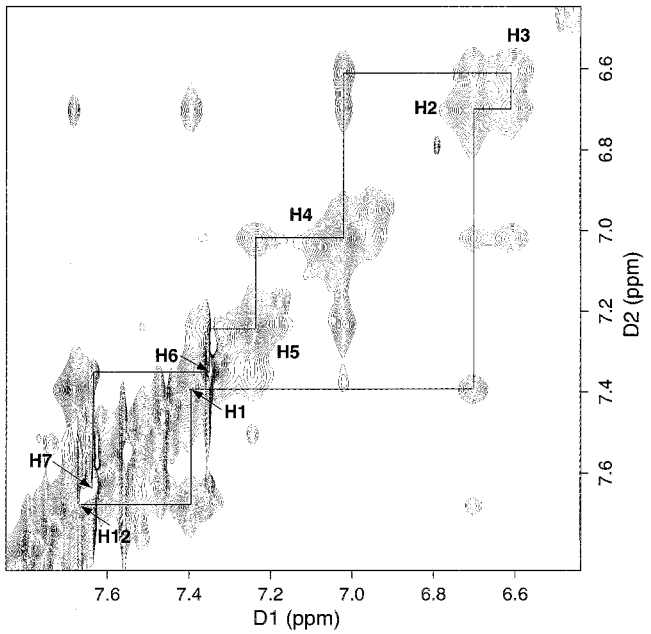

FIGURE 3: Expanded 750.13 MHz NOESY spectrum with a 250 ms mixing time showing the assignments for the aromatic protons of BA. The experiment was carried out at 20 °C.

region BP adduct (*27*). Such a correspondence was not evident on the opposite face of the PAH. Thus, for the non-bay region BA adduct, protons H12, H1, H2, and H3 exhibited a pattern of chemical shifts different from that of the bay region BP protons H11, H12, H1, and H2. The bay region ring protons H11, H12, and H1 of the BP adduct were shifted upfield into the 6.4−7.0 ppm range (*27*), whereas the non-bay region protons H12 and H1 of the non-bay region BA remained in the 7.4−7.6 ppm range (Figure 3). The chemical shift of the H12 proton of the bay region BA adduct (*29*) compared favorably with that of the bay region BP H11 and H12 protons of BP (*27*). Thus, the presence of the bay ring protons of both the BA and BP bay region adducts correlated with upfield chemical shifts. The chemical shifts of the BA resonances are listed in Table S3 of the Supporting Information.

Benz[a]anthracene−DNA NOEs. There were 20 NOEs between the BA and DNA protons. A number of NOE cross-peaks between the BA and T^{17}, the nucleotide complementary to the lesion, and C^5, the nucleotide 5′ to the lesion, are shown in Figure 4. The BA aromatic proton H7 exhibited a weak interstrand cross-peak to T^{17} CH_3. Benz[*a*]anthracene H2, H3, and H4 exhibited interstrand cross-peaks to T^{17} H2′, H2″, and H1′. These NOEs reflected the line broadening noted above for both nonexchangeable and exchangeable protons of T^{17}. Cross-peaks were observed between BA H11, located on the hydroxylated aliphatic ring at the benzylic carbon, and C^5 H2′, H2″, and H6. BA aromatic proton H12, located on the face of the BA moiety opposite from H5, H6, and H7, exhibited a NOE to C^5 H1′.

Chemical Shift Perturbations. The chemical shifts of the nonexchangeable and exchangeable protons, compared to those of the unmodified *ras61* sequence, are shown in Figure 5. The data indicated that the non-bay region adduct **1** caused minimal perturbation of the *ras61* oligodeoxynucleotide except at and immediately adjacent to the lesion. This corroborated previous findings with the bay region adducts **2** (*27*) and **3** (*29*). The greatest upfield shift of 1.4 ppm was observed for T^{17} CH_3. The imino proton of base pair C^5•G^{18} also experienced a large upfield shift of 1.1 ppm. C^5 NH_{2b} shifted upfield 0.5 ppm. C^5 NH_{2a} shifted downfield 1.0 ppm. An upfield chemical shift of 0.9 ppm was observed for T^{17}

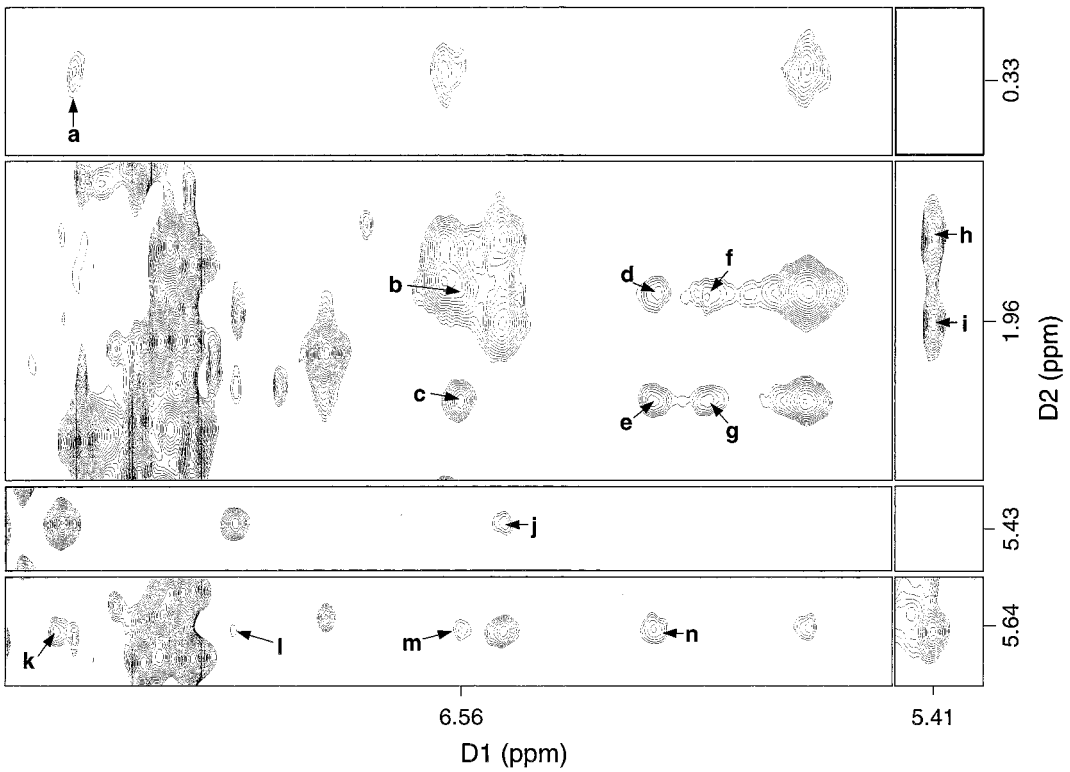

FIGURE 4: Tile plot showing NOE cross-peaks between nonexchangeable protons of DNA and BA protons: (a) T^{17} CH3 to BA H7, (b−g) T^{17} H2′ and H2″ to BA H4, H2, and H3, (h and i) C^5 H2′ and H2″ to BA H11, (j) C^5 H6 to BA H11, (k) C^5 H1′ to BA H12, and (l−n) T^{17} H1′ to BA H1, H4, and H2.

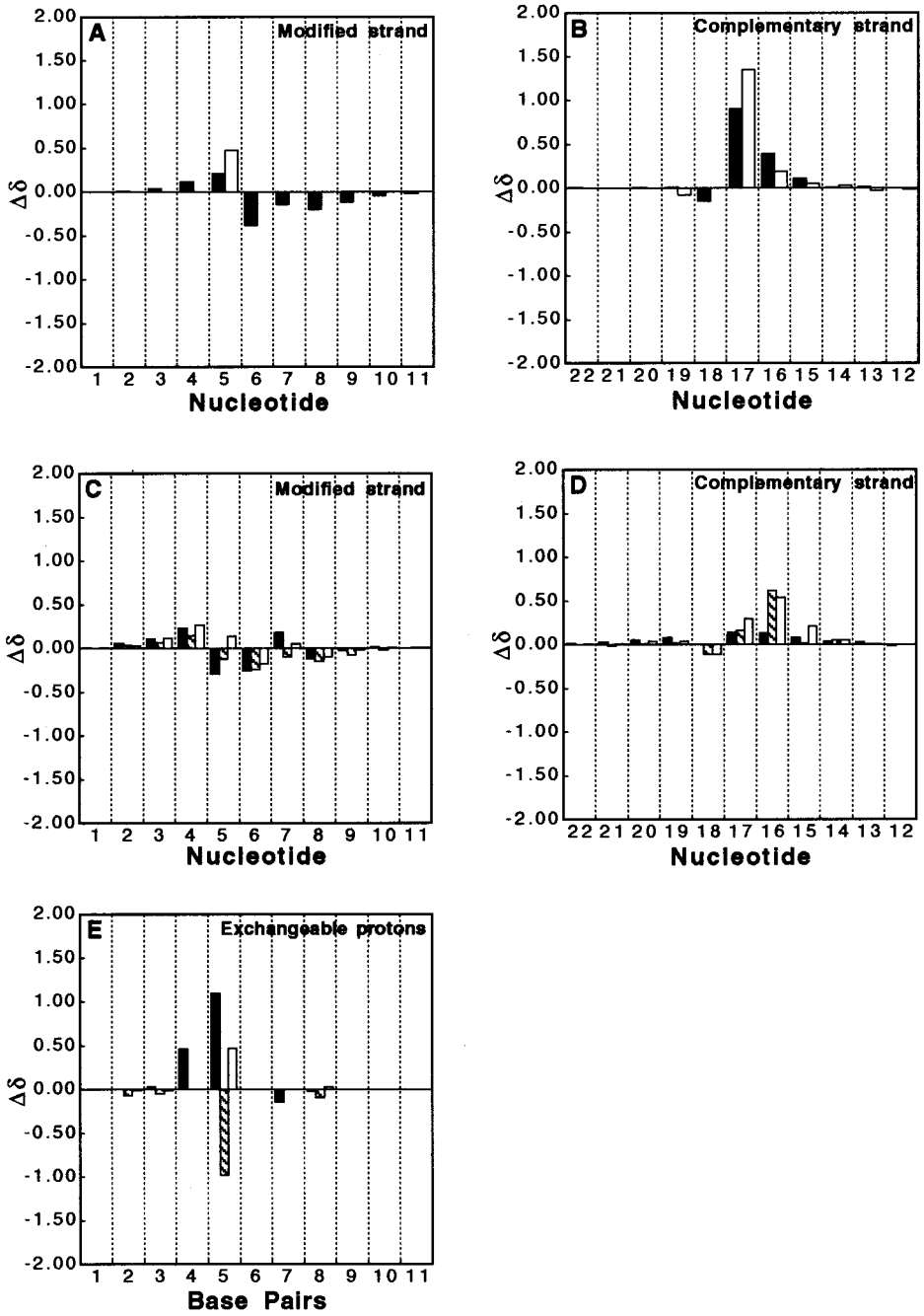

FIGURE 5: Chemical shift changes of selected protons relative to the unmodified oligodeoxynucleotide duplex. (A and B) Major groove protons in the modified and complementary strands, respectively: black bars, G/A H8 or C/T H6; white bars, C H5 or T CH_3. (C and D) Minor groove protons in the modified and complementary strands, respectively: black bars, H1′; cross-hatched bars, H2′; white bars, H2″. (E) Exchangeable protons: black bars, G N1H or T N3H; cross-hatched bars, C $N4H_{(a)}$; white bars, C $N4H_{(b)}$. $\Delta\delta = \delta_{\text{unmodified-oligodeoxynucleotide}} - \delta_{\text{modified-oligodeoxynucleotide}}$ (parts per million). Positive values correspond to upfield shifts, relative to the unmodified duplex.

H6. Upfield chemical shifts of 0.6 and 0.5 ppm were also observed for T^{16} H2′ and H2″, respectively. A 0.5 ppm upfield shift was detected for T^{19} N3H and C^5 H5. Other smaller upfield shifts were observed for a number of protons near the adduction site.

^{1}H Spectral Line Widths. Excess ^{1}H line width was observed for a number of protons adjacent to the adduct site. At 20 °C, the X^6 H8 resonance (8.49 ppm) had a line width of 31 Hz (see Figure 6), which was approximately 4 times as broad as typical ^{1}H line width values observed for adenine H8 in duplex oligodeoxynucleotides (6−8 Hz). The line width of the T^{17} CH_3 resonance (0.32 ppm) was 43 Hz, also distinctly broadened by approximately 30 Hz compared with that of T^{13} CH_3. As noted above, the imino protons of nucleotides T^{17} and T^{16} were exchange broadened to the point that they were no longer observable.

Experimental Restraints. There were 475 experimental distance restraints derived from nonexchangeable ^{1}H NOEs by MARDIGRAS. These consisted of 314 intranucleotide restraints, 125 internucleotide restraints, and 36 BA−DNA restraints. The distribution of these restraints for each base is summarized in Figure 7. The restraints were approximately evenly distributed along the length of the oligodeoxynucleotide. The smaller numbers of restraints for some nucleotides, e.g., X^6, were attributed to line broadening, resulting in a loss of NOE cross-peaks. Another exception was G^{18}, which

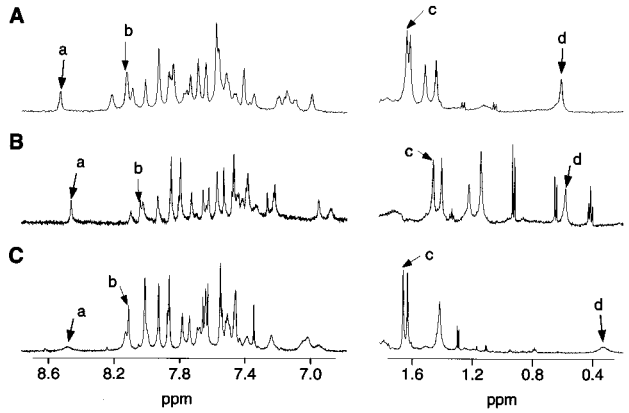

FIGURE 6: (A) ^{1}H spectrum of adduct **2**, the bay region BP-modified *ras61* sequence at 25 °C. (B) ^{1}H spectrum of adduct **3**, the bay region BA-modified *ras61* sequence at 15 °C. (C) ^{1}H spectrum of adduct **1**, the non-bay region BA-modified *ras61* sequence at 20 °C. The labels in these spectra indicate (a) the A^6 H8 resonance, (b) the A^9 H8 resonance, (c) the T^{13} CH_3 resonance, and (d) the T^{17} CH_3 resonance.

exhibited no internucleotide restraints with T^{17}. The restraints also included 55 empirical sugar pucker restraints, 35 empirical backbone angle restraints, and 18 empirical planarity restraints. A list of experimental distance restraints along with the upper and lower bounds is shown in Table S4 of the Supporting Information.

Structural Refinement. Two starting structures were used, which were built from B-DNA and A-DNA using INSIGHTII (version 97.0) such that the BA moiety intercalated between C^5•G^{18} and X^6•T^{17} (designated BA-Bi and BA-Ai). Figure 8 shows stereoviews of six rMD-generated structures based on BA-Bi and six based on BA-Ai. The stick model shown in Figure 9 represents the final refined structure obtained by averaging each family of emergent structures, followed by PEM. The refined structure was a right-handed duplex, in which the BA moiety intercalated from the major groove between C^5•G^{18} and X^6•T^{17}. The duplex suffered localized distortion at and immediately adjacent to the adduct site, evidenced by the disruption of the Watson−Crick base pairing for X^6•T^{17} and A^7•T^{16}, the increased rise of 7.7 Å between base pairs C^5•G^{18} and X^6•T^{17}, and the decreased twist of 16° relative to 36° generally observed for B-DNA between base pairs X^6•T^{17} and A^7•T^{16}. The base pair X^6•T^{17} also buckled away from the intercalated BA moiety and separated from each other indicated by −27° in buckle and −39° in opening. The calculated structures predicted that T^{17} was twisted out of plane, as indicated by 33° changes in propeller twist for X^6•T^{17}. The distortion in the duplex was localized, such that base pairs removed from the adduct remained in a B-like conformation.

The precision of the emergent structures was monitored by pairwise calculation of rms deviations (rmsds) (Table 1). The two starting structures utilized in the rMD calculations differed by 6.6 Å rmsd. When compared to the structures emergent from the rMD calculations, the BA-Ai starting structure differed from ⟨rMDAi⟩, with a rmsd of 5.7 Å, which indicated that the emergent structures did not converge to an A-DNA geometry. When compared to ⟨rMDBi⟩, the BA-Bi starting structure yielded a rmsd of 3.3 Å, suggesting that the emergent structures were more similar to B-DNA geometry. The maximum pairwise rmsd between the refined

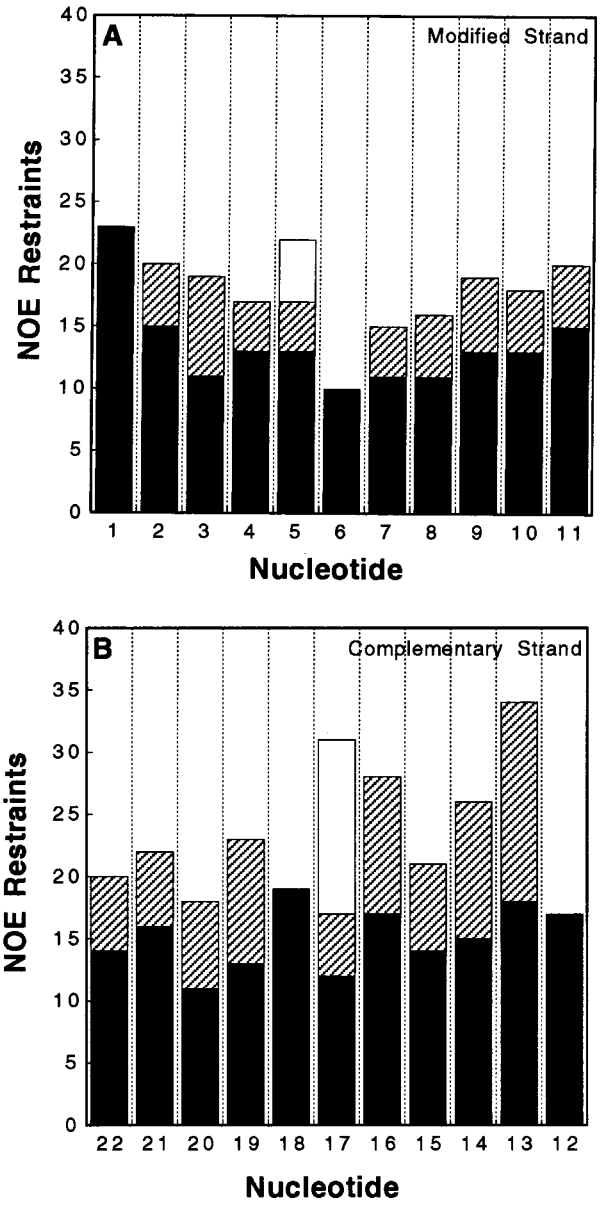

FIGURE 7: Distribution of NOE restraints applied in the structural refinement. (A) Modified strand and (B) complementary strand: cross-hatched bars, internucleotide NOEs; black bars, intranucleotide NOEs; white bars, BA−DNA NOEs. The internucleotide NOEs are counted in the direction n to $n - 1$.

structures which emerged from the sets of rMD calculations starting from BA-Ai and BA-Bi was 1.4 Å. This suggested that starting from either BA-Ai or BA-Bi, the rMD calculations converged to similar emergent structures. Control calculations which were performed using the two starting structures in the absence of the NOE restraints did not converge, which indicated that the convergence to the final structures shown in Figure 9 was due to the NOE restraints. The distribution of the individual emergent structures about the average yielded a rmsd value of <1 Å, suggesting that the experimental restraints applied to the calculations satisfactorily described a single ensemble of structures.

The accuracy of the emergent structures was assessed by complete relaxation matrix calculations (*47*). These compared theoretical NOE intensities generated from the model structures with experimental data. The results are summarized in Table 1. The R_1^x values of the starting structures BA-Ai and BA-Bi (Figure S3 of the Supporting Information)

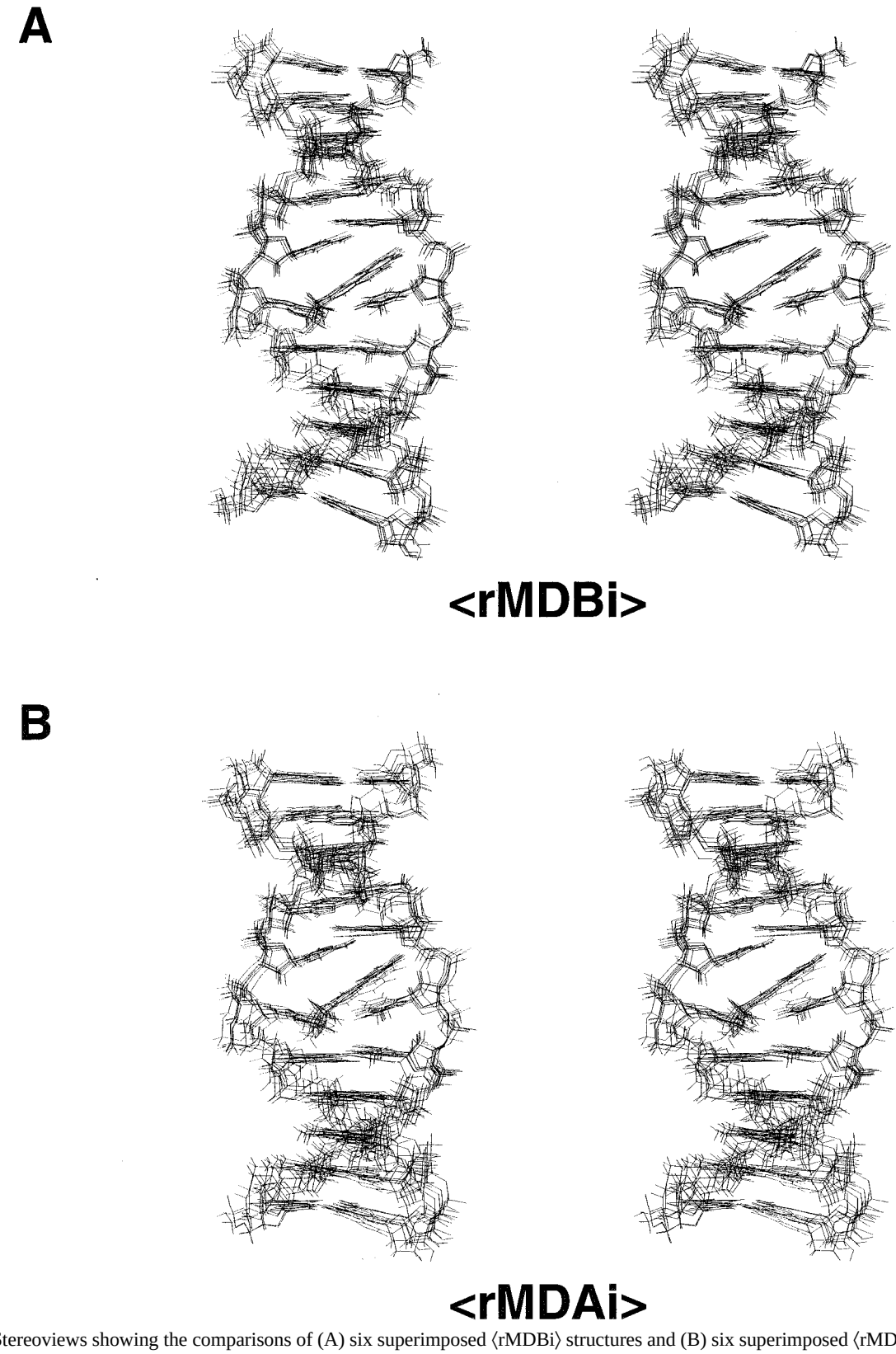

FIGURE 8: Stereoviews showing the comparisons of (A) six superimposed ⟨rMDBi⟩ structures and (B) six superimposed ⟨rMDAi⟩ structures.

indicated that the A-DNA starting structure was less consistent with the NMR data than the B-DNA starting structure. Theoretical NOE intensities from each of the refined structures yielded R_1^x values of 8.7×10^{-2} for intranucleotide NOEs and 8.5×10^{-2} for internucleotide NOEs. These were independent of the respective starting structures, which suggested that the refined structures were in improved agreement with the data. The major improvement between the starting structures and the final refined structures was observed in the internucleotide NOEs. This was consistent with the expectation that intercalation and associated unwinding of the duplex perturbed the pattern of NOEs between adjacent base pairs, but not the intranucleotide NOEs. Figure 10 details the R_1^x values as a function of nucleotide, in the adducted duplex, neglecting the terminal base pairs, which were disordered due to fraying effects. In most instances,

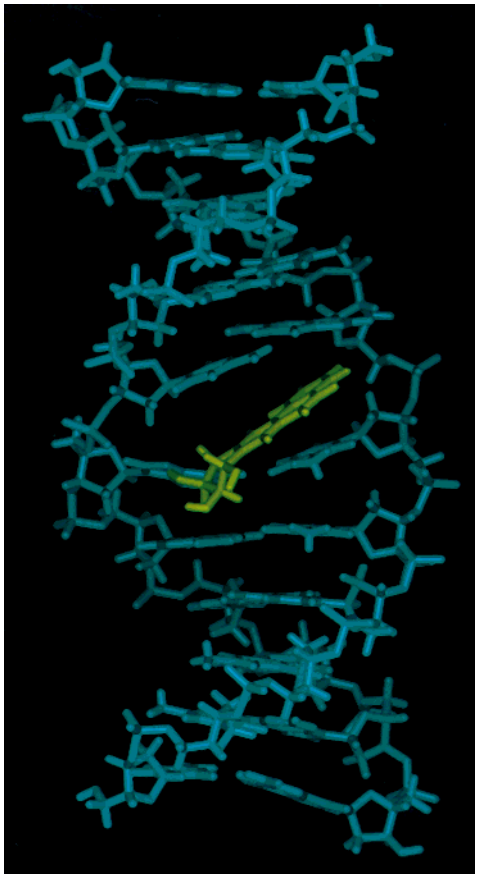

FIGURE 9: Stick model representation of the final structure, ⟨rMDav⟩, averaged from the 12 sets of two families of rMD structures, ⟨rMDAi⟩ and ⟨rMDBi⟩. The BA moiety is yellow.

the R_1^x values were found to be between 5 and 11 × 10^{-2}. This suggested that the quality of the refinement was relatively consistent at all positions in the adducted duplex.

DISCUSSION

Several observations emerged from comparison of the non-bay region BA adduct **1** with the bay region BP and BA adducts **2** and **3** with corresponding stereochemistry. The stereochemistry of the benzylic carbon determined the intercalation of these PAH adducts on the 5′-side of the modified adenine, and not the presence or absence of the bay region ring. While all of these PAH adducts at adenine N^6 intercalated, there were significant differences between the non-bay region BA adduct **1** and bay region adducts **2** (*27*) and **3** (*29*). The loss of the bay region ring resulted in changes in the geometry of base pairing, and greater disorder at the lesion site. These differences correlated with site-specific mutagenesis data, which indicated that adduct **1** was easily bypassed in vivo and was nonmutagenic, in contrast to adducts **2** and **3** that were not readily bypassed in vivo and induced A → G mutations (*37*, *58*).

Structure of the Non-Bay Region Benz[a]anthracene Lesion. Figure 9 shows the structure of the non-bay region BA adduct **1** emergent from the restrained molecular dynamics calculations. The BA moiety intercalated from the major groove, above the 5′-face of the modified adenine. This was consistent with the pattern of NOEs in the 5′-direction from the BA moiety to base pair C^5·G^{18} (Figure 11). Moreover, the normal NOE connectivity between the

Table 1: Analysis of the MD-Generated Structures of the BA Adduct **1**

NMR Restraints	
total no. of distance restraints	475
no. of interresidue distance restraints	125
no. of intraresidue distance restraints	314
no. of DNA−BA distance restraints	36
empirical restraints	
no. of H-bonding restraints	42
no. of dihedral planarity restraints	18
no. of sugar pucker restraints	55
no. of backbone torsion angle restraints	35
Structural Statistics	
NMR *R*-factor (R_1^x)[a−c]	
BA-Ai	0.17
BA-Bi	0.12
⟨rMDAi⟩	0.0853 ± 0.0006
⟨rMDBi⟩	0.0856 ± 0.0006
⟨rMDav⟩	0.0865
rmsd of NOE violations (Å)	0.037 ± 0.003
no. of NOE violations >0.1 Å in the entire duplex	21 ± 2
root-mean-square deviations from ideal geometry	
bond lengths (Å)	0.0246 ± 0.0001
bond angles (deg)	1.94 ± 0.01
improper angles (deg)	0.35 ± 0.01
pairwise rmsd (Å) over all atoms	
BA-Bi vs BA-Ai	6.59
BA-Bi vs ⟨rMDBi⟩	3.28 ± 0.14
BA-Ai vs ⟨rMDAi⟩	5.68 ± 0.33
⟨rMDBi⟩ vs ⟨rMDAi⟩	1.06 ± 0.17
⟨rMDAi⟩ vs ⟨rMDav⟩	0.80 ± 0.08
⟨rMDBi⟩ vs ⟨rMDav⟩	0.68 ± 0.07

[a] Only the inner nine base pairs were used in the calculations, to exclude end effects. The mixing time was 250 ms. All values for R_1^x are times 10^2. [b] $R_1^x = \Sigma|(a_o)_i^{1/6} - (a_c)_i^{1/6}|/\Sigma|(a_o)_i^{1/6}|$, where a_o and a_c are the intensities of observed (non-zero) and calculated NOE cross-peaks, respectively. [c] BA-Ai, starting energy-minimized A-DNA with the BA moiety intercalated between base pairs 5 and 6; BA-Bi, starting energy-minimized B-DNA with the BA moiety intercalated between base pairs 5 and 6; ⟨rMDAi⟩, average of six rMD structures starting from BA-Ai; ⟨rMDBi⟩, average of six MD structures starting from BA-Bi; and ⟨rMDav⟩, average of 12 rMD structures starting from BA-Ai and BA-Bi.

neighboring imino protons in base pairs C^5·G^{18} and X^6·T^{17} was missing. The upfield shift of 1.1 ppm for G^{18} N1H in base pair C^5·G^{18} was also consistent with intercalation. The 1.0 ppm dispersion of the BA aromatic proton chemical shifts suggested that these protons existed in significantly different electronic environments, also consistent with intercalation. To accommodate intercalation of the non-bay region BA adduct, base pair X^6·T^{17} underwent more buckling, and disruption of Watson−Crick base pairing, relative to the unmodified *ras61* oligomer. The increased rise of 7.7 Å between base pairs C^5·G^{18} and X^6·T^{17} was consistent with intercalation. The BA aromatic protons H5, H6, and H7 faced toward the major groove. They were predicted to be less influenced by the ring currents of the adjacent nucleotide bases, whereas protons H2, H3, and H4 were positioned such that ring current shielding from G^{18} was anticipated. This was consistent with the greater upfield shifts observed for the latter protons. The orientation of the BA ring resulted in localization of the NOEs between BA and DNA on the two faces of the BA ring. The BA aromatic proton H7 faced toward the major groove and exhibited a weak NOE to T^{17} CH_3. Benz[*a*]anthracene H2, H3, and H4 exhibited NOEs to T^{17} H2′, H2″, and H1′. NOEs between H11 and H12 and C^5 H2′, H2″, and H1′ were explained by the location of these

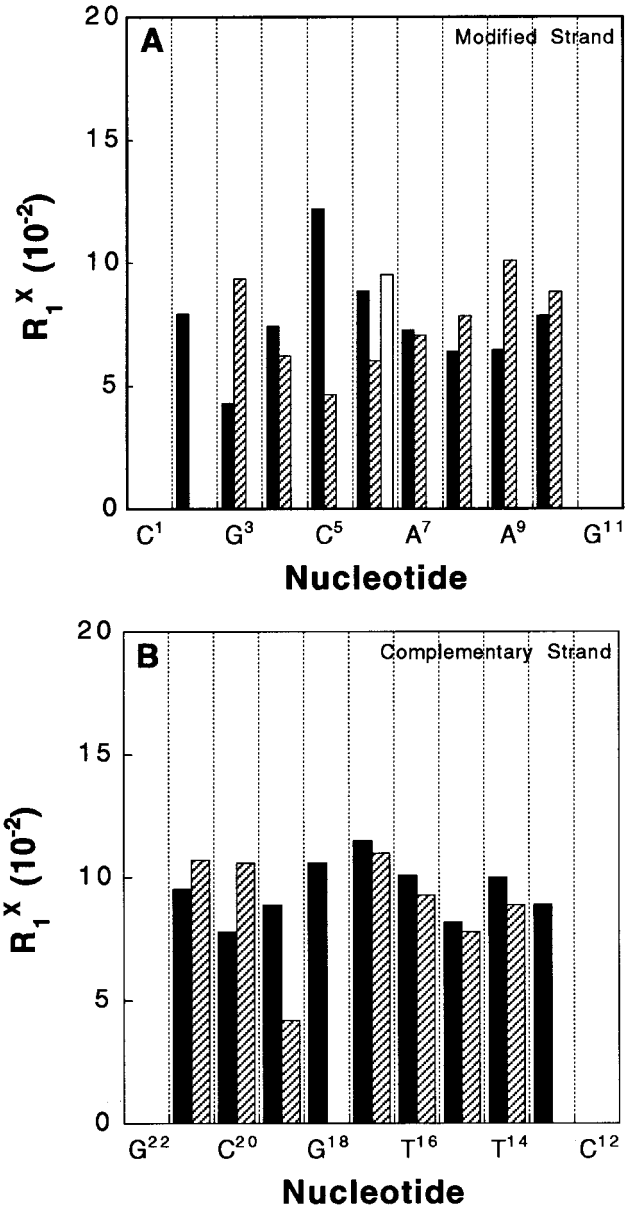

FIGURE 10: Bar diagrams showing the per-nucleotide R_1^x values for the modified and complementary strands of the BA adduct **1**. The black bars show the intranucleotide R_1^x values, the cross-hatched bars the internucleotide R_1^x values, and the white bars the interstrand R_1^x values between X^6 and T^{17}.

protons with respect to C^5. The orientation of the BA moiety explained the upfield chemical shifts of 0.9 and 1.4 ppm, observed for T^{17} H6 and CH_3, respectively. These protons both lay beneath the PAH ring. The 0.5 ppm upfield shift for C^5 H5 was explained by its orientation above the PAH ring.

Stereochemistry at the Benzylic Carbon Controls 5′-Intercalation. The bay region BP adduct **2** and the non-bay region BA adduct **1** differ in the absence of the bay region ring in adduct **1** (Chart 2). In both instances, the PAH lesion intercalated above the 5′-face of the modified adenine. Thus, the propensity toward 5′-intercalation was driven by the common stereochemistry at the benzylic carbon, and not by the presence or absence of the bay region ring. On the other hand, the missing bay region ring in adduct **1** resulted in measurable differences in its solution structure as compared with adduct **2**, or with adduct **3** (Figure 12).

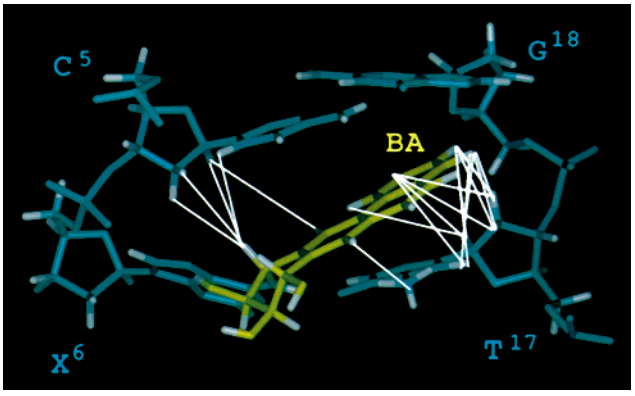

FIGURE 11: Refined structure viewing the BA moiety (yellow) from the major groove. The white lines represent NOEs, which were used in the rMD calculations.

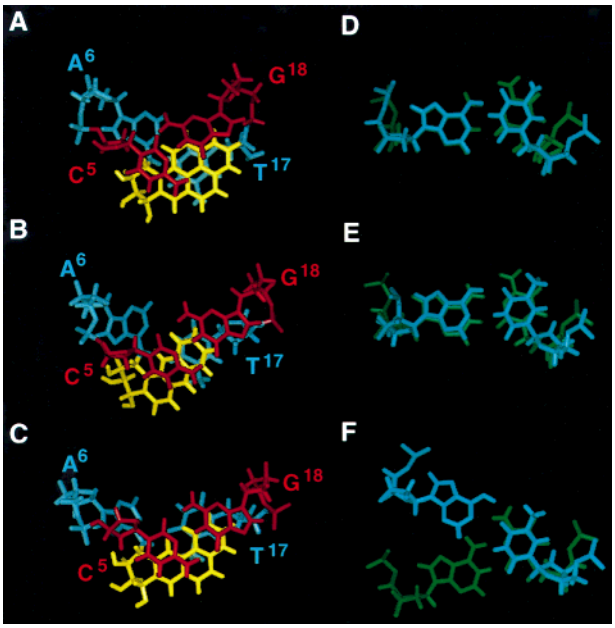

FIGURE 12: Stacking patterns of the PAH moiety (yellow) relative to DNA base pairs and structure overlap analysis. (A) Base pair C^5·G^{18} (red) above X^6·T^{17} (blue) in the BP-adducted site. (B) Base pair C^5·G^{18} (red) above X^6·T^{17} (blue) in the bay region BA-adducted site. (C) Base pair C^5·G^{18} (red) above X^6·T^{17} (blue) in the non-bay region BA-adducted site. (D) The BP-modified X^6·T^{17} base pair (blue) superimposed over the A·C mismatch base pair (green). (E) The bay region BA-modified X^6·T^{17} base pair (blue) superimposed over the A·C mismatch base pair (green). (F) The non-bay region BA-modified X^6·T^{17} base pair (blue) superimposed over the A·C mismatch base pair (green).

Poorer Stacking at the Adduct Site. Poorer base stacking between the BA moiety and the adjacent base pairs was the most evident characteristic structural feature of the non-bay region BA adduct **1**. The lack of large upfield shifts for BA aromatic protons H12 or H1 was of interest because these protons were positioned where the bay region ring normally would have been located. This contrasted with H11 and H12 of adducts **2** (*27*) and **3** (*29*), which exhibited upfield shifts. These observations suggested the role of the bay region ring in maintaining stacking interactions at the lesion site. The base pairing geometry of adduct **1** differed from that of adducts **2** and **3**. A common structure that can be discerned in Figure 12 was observed for the latter two bay region BP and BA adducts in the *ras61* oligodeoxynucleotide.[2] Both of these induced A → G mutations in site-specific mutagen-

esis experiments in vivo (*37*, *58*). The common structure was characterized by a shift of the modified adenine toward the minor groove. Consequently, the modified base pair geometry resembled the geometry of a wobble A·C pair. Significantly, adduct **1** was readily bypassed in vivo, was nonmutagenic (*37*), and did not exhibit this geometry. The failure of adduct **1** to exhibit the base pair geometry observed for the mutagenic bay region adducts was attributed in part to a reduced level of stacking interactions as a consequence of the loss of the bay region ring.

Structural Disorder of the Non-Bay Region Benz[a]-anthracene Adduct. The non-bay region BA adduct was also characterized by greater disorder at the lesion site, as compared to adducts **2** (*27*) and **3** (*29*). This conclusion was derived from a number of observations. NMR spectral evidence suggested greater line broadening at and adjacent to this adduct, as compared to that of the bay region adducts. This was observed in the spectrum of exchangeable protons. For this non-bay region adduct, the imino protons of T^{17} and T^{16} were completely exchange-broadened, indicative of increased disruption of these base pairs. The rMD calculations predicted Watson−Crick base pairing was disrupted at base pairs X^6·T^{17} and A^7·T^{16}. The disruption of Watson−Crick hydrogen bonding at A^7·T^{16} and at the adduct site (T^{17}) had not been observed for the corresponding bay region adducts (*27*, *29*). The broadening of resonances from the nonexchangeable protons of X^6 and T^{17} (Figure 1) provided further evidence of increased motional disorder for this non-bay region adduct. This also was not observed for the corresponding bay region adduct. The greater disorder of the non-bay region BA adduct was consistent with the 16 ± 1 °C reduction in T_m of the X^6-modified DNA duplex that occurred despite the intercalation of the BA moiety into the helix.

The biological consequence of increased disorder at the lesion site remains to be determined. A potential consequence is that the non-bay region BA adduct **1** may be preferentially recognized by cellular repair systems. A mechanism for the recognition of damaged DNA that involves the identification of altered base dynamics was proposed (*59*). Site-specific motional disorder was also associated with the recognition of restriction endonuclease sites (*60*). The increased disorder of the non-bay region BA adduct as compared to that of the bay region adducts may also contribute to the facile bypass of this lesion observed in vivo (*37*), perhaps providing greater degrees of freedom for the replication complex, in enabling bypass of the lesion.

Summary. The oligodeoxynucleotide carrying the non-bay region BA adduct **1** had the BA moiety intercalated from the major groove between C^5·G^{18} and X^6·T^{17}. The BA lesion increased the base step between C^5·G^{18} and X^6·T^{17} and unwound the helix. This result paralleled those from earlier studies with the corresponding bay region BP and BA adducts at this site. It suggested that the extent of 5′-intercalation was determined by the stereochemistry at the benzylic carbon. The loss of the bay region ring in adduct **1** caused two significant changes that correlated with the mutagenic consequences of these lesions. First, poorer stacking with adjacent base pairs was observed, which resulted in a base pair geometry at the lesion site that differed from those of the corresponding bay region adducts. Second, without the bay region ring, the non-bay region BA adduct exhibited greater motional disorder. This was attributed to the weaker stacking affinity of the non-bay region adduct, and may make the adduct site easily recognized by cellular repair systems.

ACKNOWLEDGMENT

We thank Mr. Markus Voehler for assistance with the collection of NMR data and Mr. Jason P. Weisenseel for assistance with processing the data. Dr. Irene Zegar and Professor R. Stephen Lloyd (University of Texas Medical Branch, Galveston, TX) provided helpful discussions.

SUPPORTING INFORMATION AVAILABLE

Tables S1−S3, which detail the ^{1}H NMR chemical shift assignments, Table S4, which shows the experimental distances and classes of restraints, Figure S1, which shows the starting structures used in the MD calculations, Figure S2, which shows atomic charges obtained for the BA lesion, and Figure S3, which shows the per-residue R_1^x values for BA-Bi and BA-Ai starting structures. This material is available free of charge via the Internet at http://pubs.acs.org.

REFERENCES

1. Grimmer, G. (1979) in *Environmental Carcinogens: Selected Methods of Analysis III*, International Agency for Research on Cancer, Lyon, France.
2. International Agency for Research on Cancer (1983) in *Monograph on the Evaluation of Carcinogenic Risk of the Chemical to Man: Certain Polycyclic Aromatic Hydrocarbons and Heterocyclic Compounds*, Lyon, France.
3. Snook, M. E., Severson, R. F., Arrendale, R. F., Higman, H. C., and Chortyk, O. (1977) *Beitr. Tabakforsch. 9*, 79−101.
4. Pott, P. (1963) *Natl. Cancer Inst. Monogr. 10*, 7−13.
5. Yang, S. K. (1988) *Biochem. Pharmacol. 37*, 61−70.
6. Guengerich, F. P., and Shimada, T. (1991) *Chem. Res. Toxicol. 4*, 391−407.
7. Dipple, A., Moschel, R. C., and Bigger, C. A. H. (1984) in *Chemical Carcinogens* (Searle, C. E., Ed.) pp 41−163, American Cancer Society, Washington, DC.
8. Geacintov, N. E. (1985) in *Polycyclic Hydrocarbons and Carcinogenesis* (Harvey, R. G., Ed.) pp 107−124, ACS Symposium Series, American Chemical Society, Washington, DC.
9. Thakker, D. R., Yagi, H., Levin, W., Wood, A. W., Conney, A. H., and Jerina, D. M. (1985) in *Bioactivation of Foreign Compounds* (Anders, M. W., Ed.) pp 177−242, Academic Press, New York.
10. Jennette, K. W., Jeffery, A. M., Blobstein, S. H., Beland, F. A., Harvey, R. G., and Weinstein, I. B. (1977) *Biochemistry 16*, 932−938.
11. Osborne, M. R., Jacobs, S., Harvey, R. G., and Brookes, P. (1981) *Carcinogenesis 2*, 553−558.
12. Dipple, A., Pigott, M., Moschel, R. C., and Costantino, N. (1983) *Cancer Res. 43*, 4132−4135.
13. Vousden, K. H., Bos, J. L., Marshall, C. J., and Phillips, D. H. (1986) *Proc. Natl. Acad. Sci. U.S.A. 83*, 1222−1226.
14. Ralston, S. L., Seidel, A., Luch, A., Platt, K. L., and Baird, W. M. (1995) *Carcinogenesis 16*, 2899−2907.
15. Harvey, R. G. (1982) *Am. Sci. 70*, 386−393.
16. Conney, A. H. (1982) *Cancer Res. 42*, 4875−4917.
17. Levin, W., Chang, R. L., Wood, A. W., Yagi, H., Thakker, D. R., Jerina, D. M., and Conney, A. H. (1984) *Cancer Res. 44*, 929−933.
18. Slaga, T. J., Huberman, E., Selkirk, J. K., Harvey, R. G., and Bracken, W. M. (1978) *Cancer Res. 38*, 1699−1704.
19. Wood, A. W., Levin, W., Lu, A. Y., Ryan, D., West, S. B., Lehr, R. E., Schaefer-Ridder, M., Jerina, D. M., and Conney, A. H. (1976) *Biochem. Biophys. Res. Commun. 72*, 680−686.
20. Wood, A. W., Chang, R. L., Levin, W., Lehr, R. E., Schaefer-Ridder, M., Karle, J. M., Jerina, D. M., and Conney, A. H. (1977) *Proc. Natl. Acad. Sci. U.S.A. 74*, 2746−2750.

21. Harvey, R. G. (1991) in *Polycyclic Aromatic Hydrocarbons: Chemistry and Carcinogeneicity*, Cambridge University Press, Cambridge, U.K.
22. Buening, M. K., Wislocki, P. G., Levin, W., Yagi, H., Thakker, D. R., Akagi, H., Jerina, D. M., and Conney, A. H. (1978) *Proc. Natl. Acad. Sci. U.S.A. 75*, 5358−5361.
23. Thakker, D. R., Levin, W., Yagi, H., Tada, M., Ryan, D. E., Thomas, P. E., Conney, A. H., and Jerina, D. M. (1982) *J. Biol. Chem. 257*, 5103−5110.
24. Lehr, R. E., Kumar, S., Levin, W., Wood, A. W., Chang, R. L., Conney, A. H., Yagi, H., Sayer, J. M., and Jerina, D. M. (1985) in *Polycyclic Hydrocarbons and Carcinogenesis*, American Chemical Society, Washington, DC.
25. Kim, S. K., Geacintov, N. E., Brenner, H. C., and Harvey, R. G. (1989) *Carcinogenesis 10*, 1333−1335.
26. Feng, B., and Stone, M. P. (1995) *Chem. Res. Toxicol. 8*, 821−832.
27. Zegar, I. S., Kim, S. J., Johansen, T. N., Horton, P., Harris, C. M., Harris, T. M., and Stone, M. P. (1996) *Biochemistry 35*, 6212−6224.
28. Zegar, I. S., Chary, P., Jabil, R. J., Tamura, P. J., Johansen, T. N., Lloyd, R. S., Harris, C. M., Harris, T. M., and Stone, M. P. (1998) *Biochemistry 37*, 16516−16528.
29. Li, Z., Mao, H., Kim, H. Y., Tamura, P. J., Harris, C. M., Harris, T. M., and Stone, M. P. (1999) *Biochemistry 38*, 2969−2981.
30. Barbacid, M. (1987) *Annu. Rev. Biochem. 56*, 779−827.
31. Cosman, M., Fiala, R., Hingerty, B. E., Laryea, A., Lee, H., Harvey, R. G., Amin, S., Geacintov, N. E., Broyde, S., and Patel, D. (1993) *Biochemistry 32*, 2488−2497.
32. Cosman, M., Laryea, A., Fiala, R., Hingerty, B. E., Amin, S., Geacintov, N. E., Broyde, S., and Patel, D. J. (1995) *Biochemistry 34*, 1295−1307.
33. Schurter, E. J., Sayer, J. M., Oh-hara, T., Yeh, H. J. C., Yagi, H., Luxon, B. A., Jerina, D. M., and Gorenstein, D. G. (1995) *Biochemistry 34*, 9009−9020.
34. Schurter, E. J., Yeh, H. J. C., Sayer, J. M., Lakshman, M. K., Yagi, H., Jerina, D. M., and Gorenstein, D. G. (1995) *Biochemistry 34*, 1364−1375.
35. Yeh, H. J. C., Sayer, J. M., Liu, X., Altieri, A. S., Byrd, R. A., Lakshman, M. K., Yagi, H., Schurter, E. J., Gorenstein, D. G., and Jerina, D. M. (1995) *Biochemistry 34*, 13570−13581.
36. Schwartz, J. L., Rice, J. S., Luxon, B. A., Sayer, J. M., Xie, G., Yeh, H. J., Liu, X., Jerina, D. M., and Gorenstein, D. G. (1997) *Biochemistry 36*, 11069−11076.
37. McNees, A. G., O'Donnell, M., Horton, P. H., Kim, H. Y., Kim, S. J., Harris, C. M., Harris, T. M., and Lloyd, R. S. (1997) *J. Biol. Chem. 272*, 33211−33219.
38. Millican, T. A., Mock, G. A., Chauncey, M. A., Patel, T. P., Eaton, M. A. W., Gunning, J., Cutbush, S. D., Neidle, S., and Mann, J. (1984) *Nucleic Acids Res. 12*, 7435−7453.
39. Harris, C. M., Zhou, L., Strand, E. A., and Harris, T. M. (1991) *J. Am. Chem. Soc. 113*, 4328−4329.
40. Kim, S. J., Harris, C. M., Koreeda, M., and Harris, T. M. (1991) *Tetrahedron Lett. 32*, 6073−6076.
41. Kim, S. J., Stone, M. P., Harris, C. M., and Harris, T. M. (1992) *J. Am. Chem. Soc. 114*, 5480−5481.
42. Kim, S. J., Jajoo, H. K., Kim, H.-Y., Zhou, L., Horton, P., Harris, C. M., and Harris, T. M. (1995) *Bioorg. Chem. 3*, 811−822.
43. Schmitz, U., and James, T. L. (1995) *Methods Enzymol. 261*, 3−44.
44. Harris, T. M., Harris, C. M., Kim, S. J., Kim, H. Y., and Zhou, L. (1994) in *Polycyclic Aromatic Compounds* (Cavalieri, E., and Rogan, E., Eds.) pp 9−16, Harwood Academic Press, Philadelphia, PA.
45. Borer, P. N. (1975) in *Handbook of Biochemistry and Molecular Biology*, CRC Press, Cleveland, OH.
46. Piotto, M., Saudek, V., and Sklenar, V. (1992) *J. Mol. Biol. 6*, 661−665.
47. Keepers, J. W., and James, T. L. (1984) *J. Magn. Reson. 57*, 404−426.
48. Borgias, B. A., and James, T. L. (1990) *J. Magn. Reson. 87*, 475−487.
49. Liu, H., Tonelli, M., and James, T. L. (1996) *J. Magn. Reson., Ser. B 111*, 85−89.
50. Brunger, A. T. (1992) in *X-Plor. Version 3.1. A System for X-ray Crystallography and NMR*, Yale University Press, New Haven, CT.
51. Brooks, B. R., Bruccoleri, R. E., Olafson, B. D., States, D. J., Swaminathan, S., and Karplus, M. (1983) *J. Comput. Chem. 4*, 187−217.
52. Nilsson, L., Clore, G. M., Gronenborn, A. M., Brunger, A. T., and Karplus, M. (1986) *J. Mol. Biol. 188*, 455−475.
53. Ryckaert, J.-P., Ciccotti, G., and Berendsen, H. J. C. (1977) *J. Comput. Phys. 23*, 327−341.
54. Clore, G. M., Gronenborn, A. M., Carlson, G., and Meyer, E. F. (1986) *J. Mol. Biol. 190*, 259−267.
55. Rinkel, L. J., Van Der Marel, G., Van Boom, J. H., and Altona, C. (1987) *Eur. J. Biochem. 163*, 287−296.
56. Ravishankar, G., Swaminathan, S., Beveridge, D. L., Lavery, R., and Sklenar, H. (1989) *J. Biomol. Struct. Dyn. 6*, 669−699.
57. Boelens, R., Scheek, R. M., Dijkstra, K., and Kaptein, R. (1985) *J. Magn. Reson. 62*, 378−386.
58. Chary, P., Latham, G. J., Robberson, D. L., Kim, S. J., Han, S., Harris, C. M., Harris, T. M., and Lloyd, R. S. (1995) *J. Biol. Chem. 270*, 4990−5000.
59. Spielmann, H. P. (1998) *Biochemistry 37*, 5426−5438.
60. Kennedy, M. A., Nuutero, S. T., Davis, J. T., Drobny, G. P., and Reid, B. R. (1993) *Biochemistry 32*, 8022−8035.

BI991607Z